Ultra-deep Keck/MOSFIRE spectroscopic observations of $z \sim 2$ galaxies: direct oxygen abundances and nebular excitation properties

Leonardo Clarke,[1] Alice Shapley,[2] Ryan L. Sanders,[3,*] Michael W. Topping,[4] Tucker Jones,[3] Mariska Kriek,[5] Naveen A. Reddy,[6] Daniel P. Stark,[4] and Mengtao Tang[4]

[1] Department of Physics and Astronomy, University of California, Los Angeles, 430 Portola Plaza, Los Angeles, CA, 90095, USA
[2] University of California, Los Angeles, 430 Portola Plaza, Los Angeles, CA, 90095, USA
[3] University of California, Davis, One Shields Ave, Davis, CA 95616, USA
[4] Steward Observatory, University of Arizona, 933 N Cherry Avenue, Tucson, AZ 85721, USA
[5] Leiden Observatory, Leiden University, P.O. Box 9513, NL-2300 AA Leiden, The Netherlands
[6] Department of Physics & Astronomy, University of California, Riverside, 900 University Avenue, Riverside, CA 92521, USA

ABSTRACT

Using deep near-infrared Keck/MOSFIRE observations, we analyze the rest-optical spectra of eight star-forming galaxies in the COSMOS and GOODS-N fields. We reach integration times of $\sim$10 hours in the deepest bands, pushing the limits on current ground-based observational capabilities. The targets fall into two redshift bins — 5 galaxies at $z \sim 1.7$ and 3 at $z \sim 2.5$ — and were selected as likely to yield significant auroral-line detections. Even with long integration times, detection of the auroral lines remains challenging. We stack the spectra together into subsets based on redshift, improving the signal-to-noise ratio on the [O III]λ4364 auroral emission line and, in turn, enabling a direct measurement of the oxygen abundance for each stack. We compare these measurements to commonly-employed strong-line ratios alongside measurements from the literature. We find that the stacks fall within the distribution of $z > 1$ literature measurements, but a larger sample size is needed to robustly constrain the relationships between strong-line ratios and oxygen abundance at high redshift. We additionally report detections of [O I]λ6302 for eight individual galaxies and composite spectra of 21 targets in the MOSFIRE pointings. We plot their line ratios on the [O III]λ5008/Hβ vs. [O I]λ6302/Hα diagnostic BPT diagram, comparing our targets to local galaxies and H II regions. We find that the [O I]/Hα ratios in our sample of galaxies are consistent with being produced in gas ionized by α-enhanced massive stars, as has been previously inferred for rapidly-forming galaxies at early cosmic times.

1. INTRODUCTION

Tracing the chemical evolution of galaxies is key to understanding how galaxy growth and evolution occur over time. The metallicity of a galaxy is influenced by numerous mechanisms such as the reprocessing of gas into heavier elements through nucleosynthesis; metal-enriched outflows driven by supernovae, AGN, and stellar winds; accretion of pristine hydrogen gas onto a galaxy; and accretion of enriched, recycled gas in the form of galactic fountains (Tumlinson et al. 2017; Davé et al. 2017). Observationally, metallicity commonly refers to the gas-phase oxygen abundance in the interstellar medium (ISM) of a galaxy since oxygen is the most abundant metal and produces strong rest-optical emission line features. The oxygen abundance in the

ISM of star-forming galaxies has been observed to correlate tightly with the stellar mass, encapsulated in what is referred to as the mass-metallicity relation (MZR). Early evidence for a MZR goes back to Lequeux et al. (1979) who measured oxygen abundances in a small sample of nearby blue compact dwarf galaxies. Later studies (e.g., Tremonti et al. 2004; Kewley & Ellison 2008; Andrews & Martini 2013) showed that there is a MZR that generally describes galaxies in the local universe. Furthermore, many works (e.g., Erb et al. 2006; Maiolino et al. 2008; Mannucci et al. 2009; Zahid et al. 2011; Steidel et al. 2014; Zahid et al. 2014; Yabe et al. 2015; Ly et al. 2016; Guo et al. 2016; Sanders et al. 2021) have revealed an evolution in the MZR with redshift, noting a change in the turnover mass and the normalization at higher z. Folding in the global star-formation rate (SFR) to the MZR yields the fundamental metallicity relation (FMR), which appears not to evolve through

cosmic time at least as far back as $z \sim 3$ (e.g., Mannucci et al. 2010; Sanders et al. 2021; Heintz et al. 2022).

The existence of these scaling relations with galaxy parameters gives insight into the processes that govern galaxy formation. The SFR, which is governed by the gas reservoir in a galaxy, is influenced by the baryon cycle, and is therefore tied to the chemical evolution in the ISM through the processes described above. Additionally, the stellar mass represents the integrated sum of star formation and is also related to the total metal production across a galaxy's lifetime. Overall, the three parameters that comprise the FMR probe the important mechanisms that determine galaxy evolution. The invariance of the FMR through a large portion of cosmic history suggests that galaxies are driven towards an equilibrium among inflow, star formation, and outflow (e.g., Davé et al. 2012; Peng & Maiolino 2014). These scaling relations are additionally useful for hydrodynamical simulations of galaxy formation since the comparison with observations provides further constraints on the subgrid physics determining the outputs (e.g., Ma et al. 2016; Davé et al. 2017; De Rossi et al. 2017; Torrey et al. 2019). Thus, measuring these galaxy parameters with high accuracy is instrumental in our understanding of galaxy formation and evolution.

Making robust measurements of the metallicity of a galaxy, however, can prove quite challenging. One of the more physically-motivated methods of determining the gas-phase oxygen abundance of a galaxy involves measuring the average electron temperature and density of its H II regions. From these physical properties, one can determine the emissivities of the emission-line transitions from each ion species which, when scaled by their respective line flux measurements, yields the abundance of each ion relative to hydrogen (i.e. O^+/H^+ and O^{2+}/H^+, see Izotov et al. 2006; Luridiana et al. 2015; Peimbert et al. 2017, for more detail). This method of abundance determination is often referred to as the "direct" method. However, to obtain the electron temperature, one must be able to detect a set of faint rest-optical auroral emission lines (e.g. [O III]λ4364, [O II]$\lambda\lambda$7322, 7332), which can be a hundred times fainter than their nebular counterparts, requiring very long exposure times (Garnett 1992; Pérez-Montero 2017). The task becomes increasingly challenging when observing targets at $z > 1$ due to the varying transmission of Earth's atmosphere in the near-infrared (i.e., rest-frame optical) and the apparent faintness of targets due to their increased distance. Additionally, in the case of the [O III]λ4364 line, whose strength relative to [O III]λ5008 is temperature-sensitive, detection becomes more difficult in higher-metallicity galaxies. This

challenge is due to the effects of more efficient metal-line cooling which leads to lower electron temperatures in the constituent H II regions in more metal-rich galaxies, rendering direct metallicity measurements much more difficult.

In light of the challenges associated with the direct method, it is common to determine metal abundances using indirect metallicity indicators which rely on the ratios of strong emission lines (e.g., Dopita et al. 2013; Pilyugin & Grebel 2016; Bian et al. 2018; Curti et al. 2020; Nakajima et al. 2022). These relations translating strong-line ratios to metallicity are calibrated to photoionization models and/or measurements of direct metallicity in H II regions and galaxies in the local universe. It is uncertain, however, whether these indirect indicators remain accurate at higher redshifts since conditions in the ISM of galaxies at earlier cosmic times may not resemble those in the local universe. Current observations suggest that galaxies at $z \sim 2$ may be characterized by harder ionizing spectra and may also have N/O ratios that vary slightly from galaxies in the local universe at fixed oxygen abundance (e.g., Shapley et al. 2015; Strom et al. 2017; Shapley et al. 2019; Heintz et al. 2022).

The evolving conditions in the ISM of galaxies has typically been traced by measurements of both high- and low-ionization emission lines (e.g., [O III]/Hβ, [N II]/Hα, [S II]/Hα). However, one low-ionization diagnostic that has been missing in analyses of galaxies at $z > 1$ is the [O I]λ6302/Hα line ratio. In studies of low-redshift galaxies, this line ratio offers insights into the hardness of the ionizing spectrum, the contribution of diffuse ionized gas (DIG), and the presence of shocks (e.g., Zhang et al. 2017). However, due to the intrinsic faintness of the [O I]λ6302 line, studies of this line diagnostic at high redshift have typically proven very difficult.

Similarly, due to the difficulty of obtaining auroral-line measurements at high redshift with ground-based facilities, there only exists a small sample of $z > 1$ galaxies in the literature for which direct oxygen abundances have been measured (examples from the literature are discussed in Sanders et al. 2020). Additionally, the integration times for most ground-based near-infrared spectroscopic surveys do not reach the required depth to achieve significant auroral-line detections. The prevalence of auroral-line detections is, however, increasing as a result of observations made by the new *James Webb Space Telescope* (JWST) (e.g., Curti et al. 2023; Nakajima et al. 2023; Sanders et al. 2023a).

The deep spectral observations analyzed in this study push the limits of ground-based, 10-m-class observatories and highlight the importance of JWST and other

future state-of-the-art observatories in characterizing galaxy properties at and beyond cosmic noon. In this study, we utilize the MOSFIRE instrument (McLean et al. 2012) on the 10-m Keck I telescope to make deep observations of a sample of eight galaxies at $z \sim 1.7-2.5$, reaching up to ~ 10 hours of integration time in some bands. We additionally produce composite spectra from this sample of eight galaxies and determine their average characteristics (i.e., chemical abundances, electron temperatures, and densities). The depth of these observations additionally enables the detection of the [O I]λ6302 feature, beyond the reach of more typical spectroscopic samples with shallower integration times (e.g., Kriek et al. 2015). Based on these measurements, we investigate the position of our sample of $z \sim 2$ galaxies in the [O III]λ5008/Hβ vs. [N II]λ6585/Hα, [S II]$\lambda\lambda$6718, 6733/Hα, and [O I]λ6302/Hα diagnostic diagrams (hereafter BPT diagrams[1]), the latter probing an unexplored parameter space at $z > 1$.

In Section 2 of this paper, we give an overview of the observational setup and data processing methods. In Section 3, we present the results of our analysis of the spectra in our sample. In Section 4, we compare our measurements with commonly-used metallicity indicators as well as consider the nature of [O I]λ6302 emission at high redshift. Throughout, we adopt the following cosmological parameters: $H_0 = 70$ km s^{-1} Mpc^{-1}, $\Omega_{\rm m} = 0.3$, and $\Omega_{\Lambda} = 0.7$. Additionally, we assume a Chabrier (2003) IMF, solar abundances of $12 + \log({\rm O/H})_\odot = 8.69$ and $12 + \log({\rm N/H})_\odot = 7.83$, and a solar metallicity of $Z_\odot = 0.014$ (Asplund et al. 2009).

2. METHODS AND OBSERVATIONS

2.1. *Sample Selection and Observation Configurations*

The target galaxies in this analysis reside in the COSMOS and GOODS-N extragalactic legacy fields covered by the CANDELS and 3D-HST surveys (Grogin et al. 2011; Koekemoer et al. 2011; Momcheva et al. 2016). These galaxies were drawn from the MOSFIRE Deep Evolution Field (MOSDEF) survey (Kriek et al. 2015) as well as the sample of extreme emission-line galaxies (EELGs) presented by Tang et al. (2019) selected from the 3D-HST WFC3 grism emission-line catalog (Momcheva et al. 2016). Targets of interest were selected based on their probability of yielding auroral-

line detections. To this effect, the target sample was composed of galaxies that had bright [O III]λ5008 emission and whose ratios among strong nebular emission lines suggested a high electron temperature based on relations observed in $z \sim 0$ H II regions (Sanders et al. 2017). Such thermal properties would result in brighter [O III]λ4364 and [O II]$\lambda\lambda$7322, 7332 auroral lines, necessary for making direct metallicity measurements. We also required galaxy targets to lie within the following redshift intervals: $1.62 \leq z \leq 1.70$, $2.32 \leq z \leq 2.61$, and $2.95 \leq z \leq 3.18$ to capture both auroral and strong nebular emission lines in the near-infrared atmospheric transmission windows covered by the Y, J, H, and K-bands.

In light of these selection criteria, we targeted a sample of 12 galaxies, which we refer to as "auroral" targets. Seven of the auroral targets were in the COSMOS field and five were in the GOODS-N field. Two of the galaxies from the COSMOS field are the subjects of a recent paper by Sanders et al. (2023b) in which their oxygen abundances were measured via the [O II]$\lambda\lambda$7322, 7332 auroral line doublet, representing the first such measurements beyond the local universe.

From the remaining sample of 10 [O III] auroral targets, two from the COSMOS field were not considered in this study. The first of these targets was excluded because the galaxy was dithered on top of an adjacent object in the field, causing the target signal to be strongly contaminated by the negative trace of its neighbor on the slit. The second of these targets was at $z = 3.12$, placing Hα beyond the coverage of the K-band, and the remaining higher-order Balmer emission lines fell onto atmospheric sky lines. As a result, it was not possible to apply Balmer-decrement-based dust corrections on this particular target. Because of these considerations, our final auroral-target sample consisted of eight galaxies: three at $z \sim 2.5$ in the COSMOS field and five at $z \sim 1.7$ in the GOODS-N field. The properties of these targets are summarized in Table 1. We utilized the multiplexing capabilities of MOSFIRE to observe an additional 29 filler targets (14 in the COSMOS pointing and 15 in the GOODS-N pointing) that we analyzed for [O I]λ6302 emission, and we refer to these targets as "non-auroral" targets.

Observations were collected over six nights: January 13, 2019 (COSMOS H-band); March 16, 2019 (COSMOS J- and H-bands); March 3, 2021 (GOODS-N J-band); March 4, 2021 (COSMOS K-band, GOODS-N J-band), April 19, 2021 (GOODS-N Y-, J-, and H-bands), and May 1, 2021 (GOODS-N H-band). The observations were taken with 0″.7 slits using an ABA'B' dither pattern, and dithered frames were aligned and combined

---

[1] BPT refers to Baldwin et al. (1981), though the [O III]λ5008/Hβ vs. [S II]$\lambda\lambda$6716, 6731/Hα diagnostic diagram was later introduced by Veilleux & Osterbrock (1987).

Table 1. [O III] auroral targets and physical properties.

ID	R.A.	Dec.	z	$\log\left(M_*/M_\odot\right)$	$\log\left(t_{age}/yr\right)$	SFR	sSFR
	(J2000)	(J2000)				$(M_\odot\ yr^{-1})$	(Gyr^{-1})
COSMOS-18812	10:00:36.896	+02:22:13.82	2.46236	$8.74^{+0.07}_{-0.04}$	$8.30^{+0.14}_{-0.18}$	$7.47^{+4.26}_{-2.53}$	13.26 ± 6.42
COSMOS-19439	10:00:24.360	+02:22:36.20	2.46598	$10.26^{+0.00}_{-0.00}$	$9.40^{+0.00}_{-0.00}$	$141.46^{+48.18}_{-34.46}$	7.90 ± 2.25
COSMOS-19753	10:00:18.182	+02:22:50.31	2.46884	$10.55^{+0.04}_{-0.00}$	$9.40^{+0.00}_{-0.06}$	$68.89^{+4.82}_{-4.54}$	1.94 ± 0.16
GOODS-N-6699	12:36:23.385	+62:10:29.04	1.66448	$9.82^{+0.05}_{-0.05}$	$9.50^{+0.00}_{-0.40}$	$11.51^{+2.62}_{-2.20}$	1.78 ± 0.42
GOODS-N-8013	12:36:52.008	+62:10:54.80	1.66776	$9.44^{+0.04}_{-0.03}$	$8.80^{+0.10}_{-0.09}$	$6.68^{+0.70}_{-0.69}$	2.43 ± 0.31
GOODS-N-8240	12:36:25.249	+62:10:58.91	1.69090	$9.76^{+0.02}_{-0.13}$	$9.20^{+0.18}_{-0.60}$	$12.36^{+9.65}_{-6.22}$	2.14 ± 1.43
GOODS-N-14595	12:36:13.373	+62:12:49.91	1.67596	$9.02^{+0.09}_{-0.05}$	$8.90^{+0.20}_{-0.50}$	$9.60^{+3.36}_{-2.29}$	9.08 ± 3.61
GOODS-N-18462	12:36:11.906	+62:13:58.80	1.67463	$9.52^{+0.05}_{-0.03}$	$9.30^{+0.11}_{-0.10}$	$3.46^{+0.30}_{-0.29}$	1.04 ± 0.13

NOTE—Some of the uncertainties on the stellar masses and ages output from FAST are quoted as being ±0.00, which only represents an uncertainty on the fitting of the models to the data. It does not account for systematic uncertainties, which were estimated to be ∼0.1 dex in a similar analysis by Muzzin et al. (2009).

to perform sky subtraction. Individual frames in the J and H bands had exposure times of 120 s, while the Y and K bands had exposure times of 180 s. The total integration times in the J, H, and K bands in the COS-MOS pointing were 1.86 h, 8.05 h, and 3.88 h respectively, while the GOODS-N pointing integration times in the Y, J, and H bands were 1.39 h, 9.71 h, and 1.06 h respectively. For COSMOS-19439 and COSMOS-19753, there were existing observations from the MOSDEF survey with 2 hours in each band. We therefore combined the deep MOSFIRE spectra with existing MOSDEF observations for these two targets, thereby increasing the total exposure time by 2 hours. The spectral resolutions in the Y, J, H, and K bands were 3400, 3000, 3650, and 3600 respectively. The median seeing for the COSMOS observations was $0\rlap{.}{''}79$, $0\rlap{.}{''}53$, and $0\rlap{.}{''}47$ in J, H, and K respectively, while the median seeing in GOODS-N was $0\rlap{.}{''}84$, $0\rlap{.}{''}61$, and $0\rlap{.}{''}67$ in Y, J, and H respectively.

2.2. *Data Reduction and Flux Calibration*

The two-dimensional (2D) reduction of the MOS-FIRE data was performed using an IDL data processing pipeline described in Kriek et al. (2015). The extractions of the 2D spectra were accomplished for each target on each mask individually using the `bmep`[2] (Freeman et al. 2019) IDL program, and we used the same slit-loss correction routine as in Reddy et al. (2015) and Kriek et al. (2015).

In order to monitor seeing conditions and carefully combine individual frames, a slit was placed on a star in each mask. Each exposure was weighted according to the observed flux of the slit star. An issue arose with the

flux calibrations from the targets on the COSMOS mask due to the fact that a galaxy in the field was dithered on top of the slit star for that mask, thereby contaminating the slit star spectrum that was used to apply the absolute flux scaling. Consequently, the default flux calibration for the COSMOS mask was unreliable. This effect had varying significance in each of the bands. In order to mitigate this source of systematic error and to ensure accurate band-to-band flux calibrations, we compared the spectra with available photometric observations and with corresponding spectral observations from the MOS-DEF survey. The existing MOSDEF spectra were taken with different slit mask configurations from those used for the new, deep observations and thus do not suffer from the same dithering issue.

The targets in the COSMOS field that had corresponding data in the MOSDEF survey were scaled multiplicatively such that the total flux of significantly-detected lines ($>5\sigma$) matched the flux of the same lines in the MOSDEF spectra. For targets on the COSMOS mask with no corresponding MOSDEF observations or without $>5\sigma$ line detections in both data sets, the spectra in each band were scaled by the average of the scaling factors on the mask in each respective filter. On average, these scaling factors adjusted the flux calibrations in each band on the order of 3-30%.

Additionally, the spectra on the GOODS-N mask were compared with existing observations in order to ensure the robustness of the flux calibrations. Since the targets on this mask did not have corresponding MOSDEF observations, the spectra in each band were scaled to agree with broad-band ground-based photometry as well as 3D-HST (Skelton et al. 2014; Momcheva et al. 2016) photometric and spectroscopic measurements.

[2] https://github.com/billfreeman44/bmep

2.3. SED and Emission-line Fitting

The spectral energy distributions (SEDs) of each target galaxy in the COSMOS field were fit across 43 photometric data points drawn from the 3D-HST catalog spanning from 3500 Å to 8 μm in the observed frame. Similarly, for the GOODS-N targets, 22 photometric points were fit across the same wavelength range. We corrected the near-IR photometric data for bright rest-frame optical emission lines using the emission-line fluxes determined from the MOSFIRE spectra analyzed in this study. The SEDs were fit with flexible stellar population synthesis models (Conroy & Gunn 2010) using the FAST fitting code (Kriek et al. 2009) in order to determine parameters such as stellar mass and age. We assumed an SMC attenuation curve with a stellar metallicity of 0.22 $Z_\odot$, a delayed-τ star-formation history of the form $t \times \exp(-t/\tau)$, and a Chabrier (2003) IMF.

We used a non-linear least squares algorithm to fit a Gaussian profile to the emission line features in each of the individual spectra as well as the stacks. Uncertainties on the line flux measurements were determined using a Monte-Carlo simulation in which each spectrum was perturbed according to the error spectrum over 100 iterations. The weaker emission-line widths were tied to the velocity widths of Hα and [O III]λ5008. Additionally, the Hα and [N II] lines were fit simultaneously, with the fluxes of [N II]λ6550 and [N II]λ6585 being tied in a ratio of 1:3 respectively. When fitting the [O I]λ6302 and [O I]λ6365 lines, they were fixed with a flux ratio of 3:1 respectively. For targets that appeared to have a broad/offset component to their emission-line profiles (e.g., non-auroral targets COSMOS-19812, 19985, 20062), we fit the brightest lines with a double Gaussian and reported only the narrow-component flux since the additional component is likely attributed to outflows or other gas not physically associated with H II regions (Leung et al. 2017). The SED fits determined from the photometry were used to model the continuum and the Balmer stellar absorption troughs. The initial, non-emission-line corrected SEDs were used to obtain a continuum fit and estimate line fluxes, and these line flux estimates were then used to correct the near-IR photometry. In turn, we re-fit the emission lines using the corrected SEDs to obtain our final line flux measurements. These line fluxes are reported along with derived physical quantities in Table 2.

2.4. Composite spectra

We found that the signal-to-noise (S/N) on [O III]λ4364 was very low ($< 2\sigma$) across most of the sample, so we created composite spectra (or "stacks")

in order to boost S/N and derive average galaxy properties for each stack. We chose to stack our sample using three different configurations that are laid out in Table 3. Stack 1 (S1), consisted of the three $z \sim 2.5$ [O III] auroral targets in the COSMOS field, stack 2 (S2) consisted of the five $z \sim 1.7$ GOODS-N auroral targets, and stack 3 (S3) consisted of all [O III] auroral targets in this study. In addition to the [O III] auroral-line stacks, we also created composite spectra that consisted of both auroral and filler targets in the MOSFIRE pointings that had coverage of the [O I]λ6302 line unaffected by atmospheric sky lines. We divided these "[O I]" stacks into two groups: a low-redshift ($1 \leq z < 2$) stack consisting of 13 targets, and a high-redshift ($2 \leq z \leq 3$) stack consisting of 8 targets.

In order to create the composite spectra, we first used the Hα/Hβ Balmer decrement and a Cardelli et al. (1989) extinction curve to correct for internal dust extinction. We then normalized each spectrum by Hα luminosity before shifting into the rest frame. Prior to stacking, each spectrum was interpolated and resampled to the same wavelength grid with 0.5 Å spacing. We then averaged together the SED models of each component spectrum after normalizing by Hα luminosity, and the resulting composite SED curve was used to model the continuum of the stacks during the line-fitting procedure. We report line luminosity measurements for each of the stacks in Table 3. Additionally, we show the stacked spectra in Figure 1 with emission lines of interest labeled.

3. RESULTS AND DETERMINATION OF PHYSICAL QUANTITIES

3.1. SFR vs. stellar mass

In Figure 2, we plot the SFRs vs. stellar masses for our sample of 8 auroral-line targets and compare them to typical values from the literature. We calculate SFRs from dust-corrected Hα luminosities using a conversion factor of 3.236×10^{-42} M$_\odot$ yr^{-1} erg^{-1} s based on models of stellar populations with sub-solar metallicity consistent with what we assume for SED fitting (Reddy et al. 2018). The galaxies in this sample agree well with the star-forming main sequence defined by larger populations of galaxies at similar redshifts. Shivaei et al. (2015) performed a linear fit to a sample of 185 galaxies in the range $1.37 \leq z \leq 2.61$, and Topping et al. (2021) fit a sample of 285 galaxies in the range $1.37 \leq z \leq 1.70$. These two empirical fits are shown as dashed and dotted black lines respectively, and they agree with the five
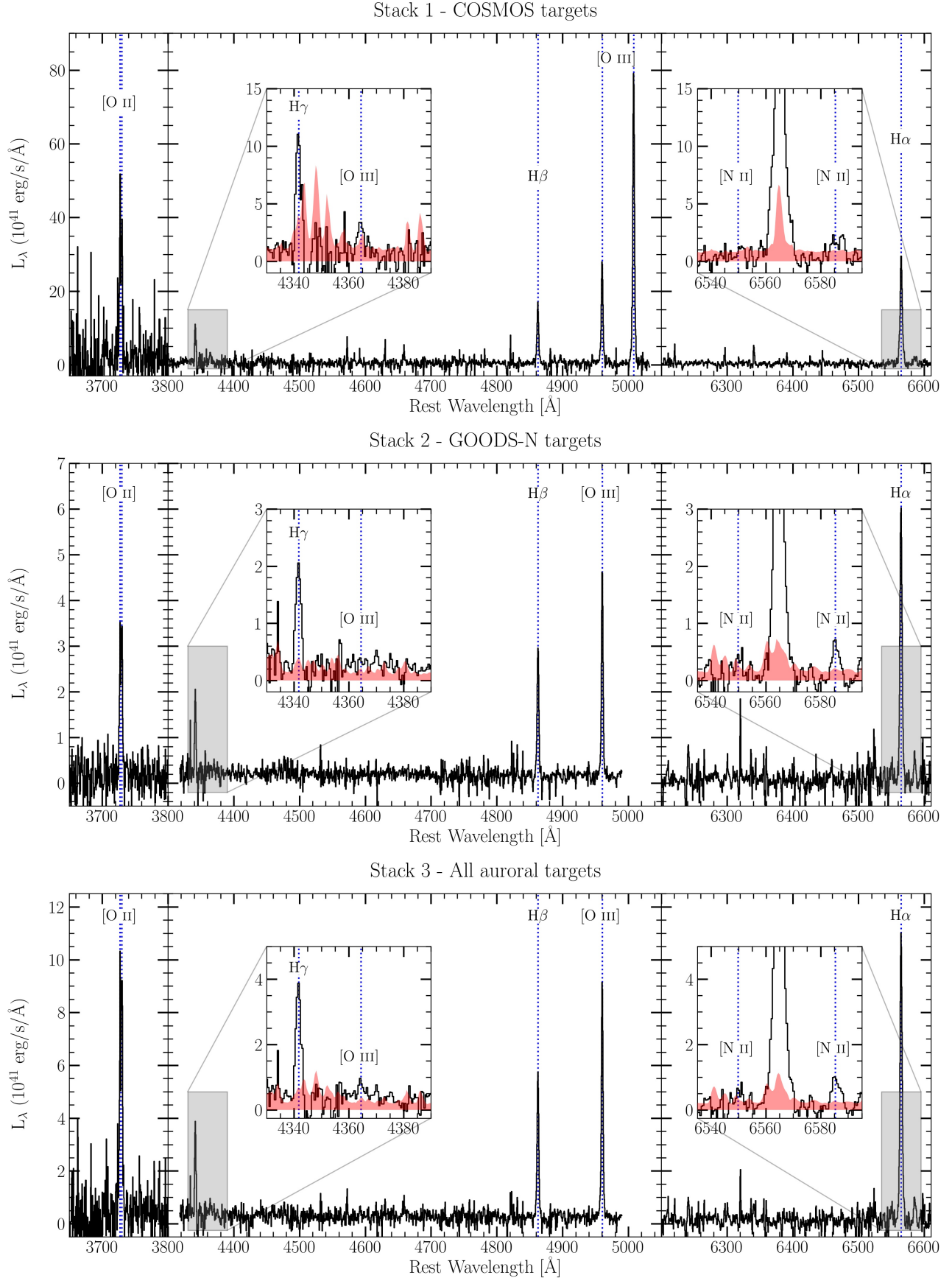
Figure 1. Composite spectra of the [O III] auroral targets. The black curve shows the luminosity density, while the error spectrum is shown in red in the inset axes. Each of the prominent emission lines is labeled and marked with a blue dotted line.

Table 2. Catalog of observed emission-line flux and physical properties for individual [O III] auroral targets.

Line	$F_{obs}(\lambda)(10^{-17}$ erg s^{-1} cm^{-2})							
	ID (COSMOS)			ID (GOODS-N)				
	18812	19439	19753	6699	8013	8240	14595	18462
[O II] λ3726	< 2.66	2.78 ± 0.71	6.37 ± 0.49	2.18 ± 0.26	3.88 ± 0.48	1.92 ± 0.42	1.29 ± 0.24	1.74 ± 0.25
[O II] λ3730	0.50 ± 0.23	2.33 ± 0.35	8.21 ± 0.55	2.58 ± 0.23	4.30 ± 0.66	2.03 ± 0.29	1.38 ± 0.21	1.82 ± 0.32
[Ne III] λ3870	$-$	< 1.52	< 1.19	< 0.60	0.55 ± 0.17	< 1.11	< 0.57	< 0.65
Hδ λ4103	$-$	$-$	$-$	0.58 ± 0.17	1.22 ± 0.30	0.57 ± 0.19	< 0.93	< 1.23
Hγ λ4342	0.58 ± 0.09	1.12 ± 0.14	2.45 ± 0.40	1.83 ± 0.21	2.10 ± 0.17	1.59 ± 0.14	1.08 ± 0.10	1.35 ± 0.20
[Fe II] λ4360*	< 0.34	0.18 ± 0.08	< 0.31	0.41 ± 0.11	< 0.78	< 0.38	< 0.24	< 0.62
[O III] λ4364*	0.34 ± 0.09	< 0.28	< 0.27	< 0.51	< 0.99	< 0.29	0.20 ± 0.06	< 0.38
[O III] λ4364	0.34 ± 0.11	< 0.28	< 0.27	< 0.51	< 0.99	0.16 ± 0.08	< 0.25	< 0.38
Hβ λ4863	1.10 ± 0.15	2.30 ± 0.08	5.88 ± 0.10	3.21 ± 0.10	4.77 ± 0.13	3.23 ± 0.22	2.24 ± 0.10	2.57 ± 0.14
[O III] λ4960	2.49 ± 0.07	3.95 ± 0.10	7.47 ± 0.22	5.29 ± 0.14	5.71 ± 0.19	4.71 ± 0.08	3.79 ± 0.08	3.71 ± 0.10
[O III] λ5008	6.99 ± 0.11	11.52 ± 0.15	21.49 ± 0.12	15.76 ± 0.41	15.61 ± 0.10	14.03 ± 0.22	11.11 ± 0.12	10.30 ± 0.11
[O I] λ6302	< 0.40	< 0.48	0.47 ± 0.09	0.26 ± 0.11	< 0.40	< 1.35	< 0.35	< 0.34
[O I] λ6365	< 0.40	< 0.63	0.15 ± 0.03	0.08 ± 0.04	< 0.37	< 1.96	< 0.32	< 0.40
[N II] λ6550	< 0.37	0.42 ± 0.12	1.01 ± 0.21	< 1.85	< 0.79	< 0.76	< 0.61	< 0.80
Hα λ6565	3.28 ± 0.14	10.89 ± 0.30	20.21 ± 0.21	11.58 ± 0.36	12.51 ± 0.79	12.22 ± 1.35	7.07 ± 0.17	5.41 ± 0.24
[N II] λ6585	< 0.33	1.27 ± 0.23	3.03 ± 0.26	1.55 ± 0.29	1.24 ± 0.28	1.13 ± 0.35	< 0.54	0.55 ± 0.23
[S II] λ6716	$-$	< 0.61	1.85 ± 0.25	< 2.56	1.90 ± 0.68	< 3.12	0.56 ± 0.21	$-$
[S II] λ6731	$-$	0.90 ± 0.25	1.66 ± 0.26	0.76 ± 0.22	< 1.15	< 17.44	< 1.22	$-$
E(B-V)$_{gas}$	$0.04^{+0.16}_{-0.13}$	$0.51^{+0.05}_{-0.05}$	$0.19^{+0.02}_{-0.02}$	$0.23^{+0.04}_{-0.04}$	0.00	$0.29^{+0.12}_{-0.14}$	$0.10^{+0.05}_{-0.05}$	0.00
T_e(O^{2+}) (10^4 K)	$2.11^{+0.29}_{-0.39}$	< 1.42	< 1.13	< 2.41	< 2.29	$1.30^{+0.24}_{-0.25}$	< 1.86	< 1.66
T_e(O$^+$) ($\times 10^4$ K)	$1.77^{+0.26}_{-0.25}$	< 1.30	< 1.09	< 1.99	< 1.90	$1.20^{+0.20}_{-0.20}$	< 1.61	< 1.46
n_e (10^2 cm^{-3})	$-$	$10.70^{+12.55}_{-6.84}$	$1.61^{+1.32}_{-0.98}$	$4.20^{+2.20}_{-2.79}$	$5.26^{+4.77}_{-3.34}$	$5.06^{+4.97}_{-3.26}$	$5.38^{+6.53}_{-3.12}$	$5.57^{+6.11}_{-3.41}$
12 + log (O$^+$/H)	$-$	> 7.78	> 7.89	> 6.89	> 6.85	$7.49^{+0.32}_{-0.24}$	> 6.99	> 6.98
12 + log (O^{2+}/H)	$7.54^{+0.19}_{-0.13}$	> 7.77	> 7.94	> 7.27	> 7.18	$7.82^{+0.28}_{-0.19}$	> 7.50	> 7.56
12 + log (O/H)	$-$	> 8.08	> 8.22	> 7.42	> 7.35	$8.02^{+0.24}_{-0.17}$	> 7.62	> 7.66
12 + log (N$^+$/H)	$5.83^{+0.30}_{-0.47}$	> 6.57	> 6.85	> 6.28	> 6.18	$6.53^{+0.24}_{-0.21}$	> 5.85	> 6.39
12 + log (N/H)	$6.71^{+0.52}_{-0.61}$	> 6.86	> 7.18	> 6.82	> 6.67	$7.05^{+0.29}_{-0.26}$	> 6.49	> 7.07
log (N/O)	$-$	$-$	$-$	$-$	$-$	$-0.99^{+0.22}_{-0.23}$	$-$	$-$

* These line fluxes for [Fe II]λ4360 and [O III]λ4364 are determined by fitting a double Gaussian simultaneously to both features, whereas the [O III]λ4364 flux without an asterisk is determined by fitting a single Gaussian profile.

** Since the [O II] doublet was affected by sky lines in this target, we estimate the O^{2+}/H abundance assuming a density of 100 cm^{-3}.

NOTE—Non-detections are reported as 2σ upper limits, and Balmer line ratios that yield negative values of E(B-V) are set to 0.00. Oxygen abundances are determined from the single-Gaussian fit to [O III]λ4364.
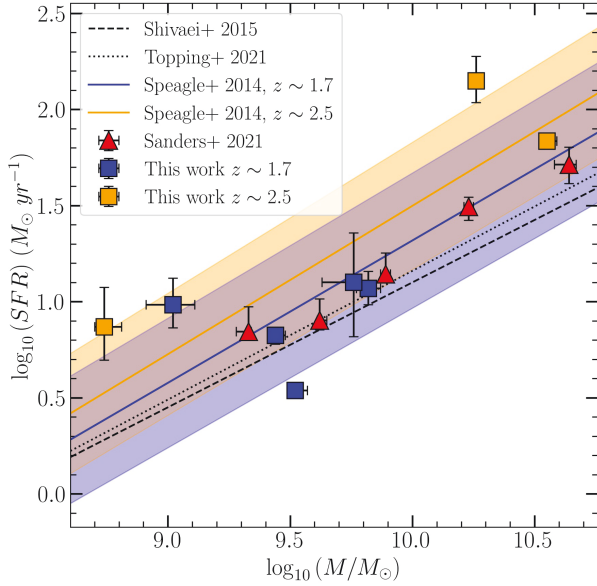
Figure 2. SFR vs. stellar mass. The colored squares indicate the auroral-line targets included in this study, with blue and orange corresponding to $z \sim 1.7$ and $z \sim 2.5$, respectively. The dashed black line shows a linear fit from Shivaei et al. (2015), while the solid blue and orange lines show the $z \sim 1.7$ and $z \sim 2.5$ SFR vs. stellar mass relations respectively from Speagle et al. (2014). The 1-σ scatter for each main sequence line is shaded in its respective color. The red triangles represent spectral stacks of $z \sim 2.3$ galaxies from Sanders et al. (2021).

GOODS-N galaxies at $z \sim 1.7$ with the exceptions of GOODS-N-18462 and GOODS-N-14595, which are offset in log(SFR) by roughly -0.3 dex and +0.6 dex respectively. We additionally plot two main sequence relations defined by Speagle et al. (2014) at the median redshifts of our COSMOS and GOODS-N samples shown in orange and blue, respectively. As an additional point of reference, we overplot a sample of 280 $z \sim 2.3$ galaxies distributed among five stacks by Sanders et al. (2021), and we re-scale the stacks to use the same $H\alpha$ to SFR conversion factor we utilize in this study. For both the $z \sim 1.7$ and $z \sim 2.5$ galaxies in this study, we find agreement within 1σ relative to the respective main sequence fits with the exception of GOODS-N-18462, which falls slightly below the $z \sim 1.7$ relation. Overall, this sample of galaxies is relatively representative in terms of SFR at fixed stellar mass based on larger samples in the same redshift range.

3.2. *Abundance Determinations*

Throughout this paper, we refer to "direct" oxygen abundances as those derived from determining the ion emissivities based on electron temperature and density measurements as opposed to "indirect" methods, which

Table 3. Catalog of observed emission-line luminosities and physical properties for stacked spectra.

	$L_{obs}(\lambda)(10^{41}\ erg\ s^{-1})$		
	Stack ID		
Line	S1	S2	S3
	COSMOS	GOODS-N	Full sample
[O II] $\lambda3726$	88.13 ± 28.17	6.78 ± 1.17	19.58 ± 5.00
[O II] $\lambda3730$	89.12 ± 24.34	8.15 ± 1.11	21.86 ± 3.36
[Ne III] $\lambda3870$	–	< 1.36	–
Hδ $\lambda4103$	–	< 1.60	–
Hγ $\lambda4342$	27.21 ± 4.52	4.46 ± 0.52	9.23 ± 0.90
[Fe II] $\lambda4360^*$	< 12.91	< 1.15	1.87 ± 0.84
[O III] $\lambda4364^*$	7.56 ± 3.21	< 0.76	1.40 ± 0.46
[O III] $\lambda4364$	7.57 ± 2.71	< 0.50	1.39 ± 0.40
Hβ $\lambda4863$	49.78 ± 4.91	9.16 ± 0.50	17.38 ± 0.94
[O III] $\lambda4960$	76.66 ± 8.72	13.19 ± 0.90	26.04 ± 1.33
[O III] $\lambda5008$	255.96 ± 24.15	–	–
[O I] $\lambda6302$	< 5.08	< 0.74	< 0.81
[O I] $\lambda6365$	< 5.44	< 0.25	< 0.27
[N II] $\lambda6550$	3.21 ± 0.74	0.62 ± 0.10	1.08 ± 0.16
Hα $\lambda6565$	110.87 ± 6.29	24.01 ± 1.25	43.23 ± 1.47
[N II] $\lambda6585$	9.63 ± 2.23	1.85 ± 0.29	3.25 ± 0.47
[S II] $\lambda6716$	–	–	–
[S II] $\lambda6731$	–	–	–
$\log(M_*/M_{\odot,avg})$	9.85 ± 0.04	9.51 ± 0.06	9.64 ± 0.04
$T_e(O^{2+})\ (10^4\ K)$	$1.96^{+0.33}_{-0.37}$	< 1.27	$1.44^{+0.19}_{-0.19}$
$T_e(O^+)\ (10^4\ K)$	$1.67^{+0.26}_{-0.26}$	< 1.19	$1.30^{+0.15}_{-0.15}$
$n_e\ (10^2\ cm^{-3})$	$8.68^{+14.23}_{-6.29}$	$3.14^{+3.55}_{-2.14}$	$4.65^{+5.99}_{-3.17}$
$12 + \log(O^+/H)$	$7.41^{+0.26}_{-0.22}$	> 7.49	$7.53^{+0.22}_{-0.18}$
$12 + \log(O^{2+}/H)$	$7.43^{+0.21}_{-0.16}$	> 7.85	$7.72^{+0.17}_{-0.15}$
$12 + \log(O/H)$	$7.75^{+0.20}_{-0.15}$	> 8.01	$7.96^{+0.15}_{-0.12}$
$12 + \log(N^+/H)$	$6.13^{+0.16}_{-0.17}$	> 6.44	$6.31^{+0.15}_{-0.12}$
$12 + \log(N/H)$	$6.46^{+0.18}_{-0.18}$	> 6.96	$6.73^{+0.12}_{-0.11}$
$\log(N/O)$	$-1.30^{+0.17}_{-0.19}$	–	$-1.22^{+0.11}_{-0.12}$

* These line luminosities for [Fe II]$\lambda4360$ and [O III]$\lambda4364$ are determined by fitting a double Gaussian simultaneously to both features, whereas the [O III]$\lambda4364$ luminosity without an asterisk is determined by fitting a single Gaussian profile. Oxygen abundances are determined from the single-Gaussian fit to [O III]$\lambda4364$.

NOTE—Non-detections are reported as 2σ upper limits.

use the ratios of strong nebular emission lines empirically calibrated to local direct measurements or photoionization models. The direct method of oxygen abundance approximates a galaxy as a single H II region and thus characterizes electron temperatures and densities based on globally-integrated spectra. In this H II region approximation, it is conventional to further define two temperatures: the temperature associated with the high-ionization state and the low-ionization state of the ions of interest (e.g., $T_e(O^{2+})$ and $T_e(O^+)$, respectively). Since the energy required to ionize neutral oxygen is similar to that of hydrogen, we expect that nearly all of the oxygen within H II regions is ionized, either in the singly or doubly-ionized state, with negligible amounts

in higher ionization or neutral states. Therefore, in order to determine the oxygen abundance directly, we sum the abundances of oxygen in its two most prevalent ionization states:

$$\frac{O}{H} \approx \frac{O^+}{H^+} + \frac{O^{2+}}{H^+} \quad (1)$$

Determining the abundances of each ionization species requires knowledge of the electron temperatures and densities associated with the respective ionization zones. In the O^{2+} zone, this can be achieved through measurements of the [O III]$\lambda\lambda 4960, 5008$ and the [O III]$\lambda 4364$ lines, where the [O III]$\lambda 4364$ transition originates from a different upper energy level than the [O III]$\lambda\lambda 4960, 5008$ transitions. In turn, measuring the ratios of these lines allows one to determine the electron temperature associated with the O^{2+} zone. The same can be achieved for the O^+ ion, using the [O II]$\lambda\lambda 3727, 3730$ and [O II]$\lambda\lambda 7321, 7332$ lines which arise from different respective upper energy levels. One of the major challenges in determining direct oxygen abundances, however, is that the auroral lines produced by transitions from the upper energy levels are often intrinsically very faint, and their detection becomes the main limiting factor in obtaining direct abundance estimates. Ideally, one would measure the nebular and the corresponding faint auroral emission lines originating from the O^+ and O^{2+} ions to directly determine the electron temperature for both ionization zones. However, since our sample of [O III] auroral targets does not have coverage of the auroral [O II] lines, we employ the following theoretical relation presented by Campbell et al. (1986) to infer $T_e(O^+)$:

$$T_e(O^+) = 0.7 \times T_e(O^{2+}) + 3000 \, \text{K} \quad (2)$$

When converting a $T_e(O^+)$ measurement to $T_e(O^{2+})$, observations suggest an intrinsic scatter of approximately 1300 K in the Campbell et al. (1986) relation (Berg et al. 2020; Rogers et al. 2021). Since we are instead converting $T_e(O^{2+})$ to $T_e(O^+)$ using equation 2, we adopt an intrinsic scatter of 0.7×1300 K = 910 K, and add this in quadrature when determining the uncertainty on $T_e(O^+)$.

Electron temperatures, densities, and ionic abundances were determined using the `PyNeb` package (Luridiana et al. 2015). In order to compute the electron density n_e, we used the `getCrossTemDen()` method to simultaneously solve for $T_e(O^{2+})$ and n_e, taking the [O II]$\lambda 3727$/[O II]$\lambda 3730$ ratio to be the density-sensitive tracer. With the output values of T_e and n_e from `getCrossTemDen()`, we computed the ionic abundances using the `getIonAbundance()` method, using the ratios

of [O III]$\lambda 4959$ and [O II]$\lambda 3727, 3730$ relative to Hβ to compute the O^{2+}/H^+ and the O^+/H^+ abundances, respectively.

We additionally calculated the nitrogen abundance in our galaxy sample since we have coverage of the [N II]$\lambda 6585$ line in all targets. The nitrogen abundance is ideally determined based on emission lines arising from the N^+ and N^{2+} ions. However, we do not have coverage and/or detection of the necessary [N III] emission lines, so we make the following approximation:

$$\frac{N}{H} \approx \frac{N^+}{H^+} \times \text{ICF(N)}$$

where ICF(N) is the ionization correction factor accounting for higher ionization states, and it is defined as ICF(N) = N/N^+. We approximate this ratio as $N/N^+ \approx O/O^+$ since oxygen and nitrogen have similar ionization energies (Peimbert 1967).

One can directly measure the temperature within the N^+ zone by measuring the auroral-to-nebular line ratio [N II]$\lambda 5756$/[N II]$\lambda 6585$, analogous to the [O III]$\lambda 4364$/[O III]$\lambda 5008$ ratio for the O^{2+} zone. However, we do not have coverage of the [N II]$\lambda 5756$ line in our spectra, so we make the approximation that $T_e(N^+) \approx T_e(O^+)$. We also use the same electron density as that determined during the calculation of the oxygen abundance. We then used `getIonAbundance()` employing the [N II]$\lambda 6585$/Hβ ratio as the input to calculate the N^+/H^+ abundance. The derived constraints on density, temperature, and ionic and total abundances are reported in Table 2 for the individual targets and Table 3 for the composites.

3.3. Auroral-line Detections

The [O III]$\lambda 4364$ line was detected at greater than 2σ significance in only two targets: COSMOS-18812 and GOODS-N-8240. For COSMOS-18812, the [O II]$\lambda\lambda 3727, 3730$ line doublet fell onto a pair of sky lines, so it was not possible to constrain the electron density or the O^+ abundance. We tentatively detect [O III]$\lambda 4364$ emission in GOODS-N-8240 since the Gaussian fit to the line profile places the significance of this detection at the $>2\sigma$ level. Upon visual inspection, we report the presence of emission lying a few angstroms blueward of the [O III]$\lambda 4364$ line in two of the targets: GOODS-N-6699 and GOODS-N-14595. For GOODS-N-6699, there is an emission feature detected at $>3\sigma$ significance when centering a Gaussian profile at 4360 Å. It is uncertain whether this emission is associated with the [O III]$\lambda 4364$ line though it appears at a similar wavelength. The emission-line feature adjacent to [O III]$\lambda 4364$ in GOODS-N-14595 appears to be more
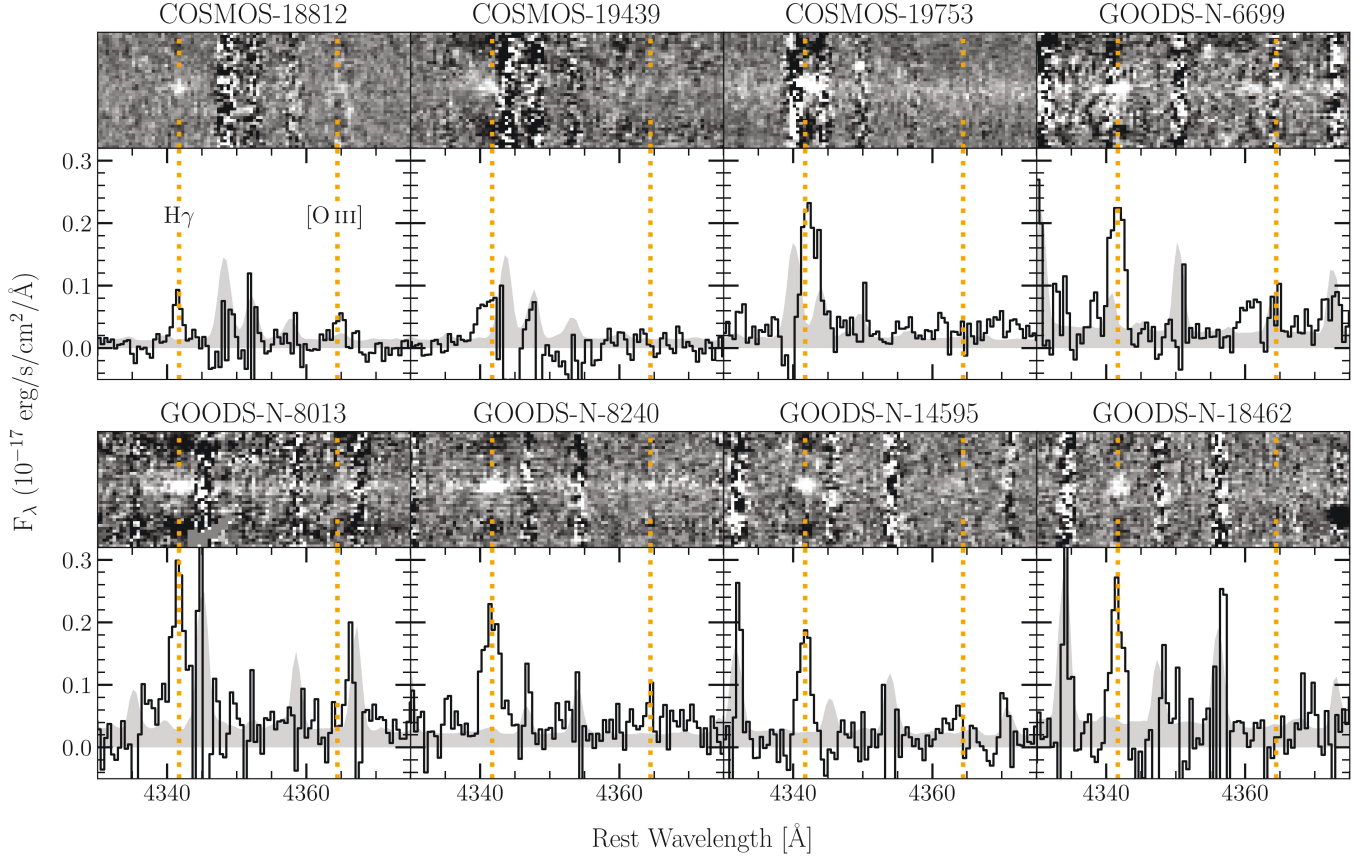
Figure 3. 2D and 1D spectra of the eight [O III] auroral targets in this study. These spectral plots span from 4335 Å to 4370 Å, covering the Hγ and [O III]λ4364 emission lines. The solid black line shows the flux density, and the shaded gray spectrum is the error on the flux density. We detect [O III]λ4364 (labeled with an orange dotted line) in COSMOS-18812 and GOODS-N-8240; however, we report emission blueward of 4364 Å in the GOODS-N 6699 and 14595 spectra.

closely centered on the expected central wavelength for the auroral oxygen line, with a significance of just 0.38σ when centering on 4360 Å. The spectra of these objects in this wavelength region can be seen in Figure 3.

Curti et al. (2017) find a similar feature in a sample of spectral stacks and attribute it to a forbidden transition of singly-ionized iron. They also suggest that the strength of this 4360 Å contamination increases with increasing galaxy metallicity. However, we do not expect this contaminating feature to have a significant impact on our spectra given that strong-line metallicity indicators of our target sample suggest our targets are half solar metallicity or less. For completeness, we report [O III]λ4364 measurements of the stacked spectra in two ways: fitting the emission around 4364 Å as a single Gaussian and fitting the feature at 4360 Å separately from [O III]λ4364. As a shorthand, we refer to the feature at 4360 Å as [Fe II]λ4360, and the simultaneous [O III] and [Fe II] line fits are denoted by an asterisk (*) in both Tables 2 and 3.

In Table 2, we see that in most cases, choosing a single vs. a double fit does little to change the [O III]λ4364

flux. The exceptions to this are GOODS-N-8240 and GOODS-N-14595 where, in the former, the single fit yields a higher S/N ratio and, in the latter, the double fit yields a better S/N ratio. Since it is unclear to what extent the emission in GOODS-N-14595 can be attributed to [O III]λ4364, we report the determination of physical quantities from the single-Gaussian fit to [O III]λ4364.

We perform this same exercise on the stacked spectra and report the results in Table 3, with the simultaneous double Gaussian fits marked by asterisks. Since the emission at 4360 Å is only seen in GOODS-N targets, we check to see if the fitting technique has an effect on the measured line luminosities in stacks 2 and 3, finding that there is no significant effect on either stack. We do see an effect on stack 1 in that the single fit has a higher S/N ratio. Thus, we use the single Gaussian fit to [O III]λ4364 in the stacks to determine physical conditions.

For the individual [O III] auroral targets, only GOODS-N-8240 has a well-constrained oxygen abundance of $12 + \log(\text{O/H}) = 8.02^{+0.24}_{-0.17}$, corresponding to $\sim21\%$ of the solar oxygen abundance. For the compos-

ite spectra, we find that the $z \sim 2.5$ COSMOS stack has an oxygen abundance of $\sim 11\%$ the solar value, while the $z \sim 1.7$ GOODS-N stack has an oxygen abundance greater than $\sim 21\%$ the solar value. For nitrogen, the abundances relative to the solar value are $\sim 4\%$ and $\gtrsim 13\%$ for stacks 1 ($z \sim 2.5$) and 2 ($z \sim 1.7$).

4. DISCUSSION

We now turn to an analysis of the emerging trends in relations between strong-line ratios and direct oxygen abundance at high redshift enabled by our deep MOS-FIRE observations. In addition, the new analysis of the [O I]$\lambda 6302$/Hα ratio in 21 galaxies beyond the local universe, while not representing a complete statistical sample, hints at the properties of the ionized gas and the stellar populations in high-redshift galaxies.

4.1. *Indirect Metallicity Indicators*

Analyzing the accuracy of indirect metallicity indicators out to high redshifts is important for our understanding of the chemical evolution of galaxies across cosmic time. With our oxygen abundance measurements of the stacked spectra of auroral targets, we have constraints for the average metallicities of the galaxies considered in this study. We compare these stacks alongside measurements from the literature to strong-line metallicity indicators in order to understand how the accuracy of these indicators may shift with cosmic time.

In Figure 4, we show six strong-line ratios vs. oxygen abundance for our three stacks, and we plot the metallicity relations from Curti et al. (2020) determined from stacks of galaxy spectra in the local universe. The short-hand labels for the strong-line ratios are defined as follows: R3 = [O III]$\lambda 5008$/Hβ, R2 = [O II]$\lambda\lambda 3727, 3730$/H$\beta$, R23 = ([O III]$\lambda\lambda 5008, 4960$ + [O II]$\lambda\lambda 3727, 3730$)/H$\beta$, O32 = [O III]$\lambda 5008$/[O II]$\lambda\lambda 3727, 3730$, N2 = [N II]$\lambda 6585$/H$\alpha$, O3N2 = ([O III]$\lambda 5008$/H$\beta$)/([N II]$\lambda 6585$/H$\alpha$). We note that below an oxygen abundance of $12 + \log{(\mathrm{O/H})} \approx 8.1$, there are fewer individual $z \sim 0$ SDSS galaxies with $>10\sigma$ [O III]$\lambda 4364$ detections, and the sample is biased toward higher specific SFR, representing a population more similar to our high-redshift sample than $z \sim 0$ galaxies (refer to the discussion in the appendix of Sanders et al. (2021) for a detailed analysis of the low-metallicity Curti et al. (2017, 2020) calibration sample). Additionally, we show the relationships between strong-line ratios and metallicity determined by Bian et al. (2018) for local galaxies selected to have emission-line properties analogous to those of high-redshift galaxies. Alongside these two line-ratio relations, we show the strong-line ratio vs. oxygen abundance for a large

sample of H II regions from the literature (compiled by Sanders et al. (2017) with data from Pilyugin & Grebel (2016), Croxall et al. (2015), and Toribio San Cipriano et al. (2016)) with a running median displayed as a solid black curve, and 1σ intervals shown as dotted lines to visualize the spread of the distribution.

Upon visual inspection, the oxygen abundances of the stacks lie within the distribution of galaxies from the literature (compiled by Sanders et al. (2020) with two additional galaxies from Sanders et al. (2023b)) shown as blue points. In the cases of log(R23) and log(N2), the Bian et al. (2018) curve serves as a better metallicity indicator to high-redshift galaxies compared to the Curti et al. (2020) curves. In the cases of the log(R3), log(R2), log(O3O2), and log(O3N2) curves, the spread of galaxies is large compared to the differences between the Curti et al. (2020) and Bian et al. (2018) curves, so it is difficult to determine if there is a preference for one over the other. In general, the stacks agree most consistently with the distribution of H II regions, though the galaxies from the literature are offset from the H II regions to higher log(R3) and log(R23) at fixed oxygen abundance.

With a small existing sample size, it is difficult to make definitive conclusions about the accuracy of these strong-line ratios, especially considering that the sample of galaxies is biased towards bright, high electron temperature targets. For two of the individual auroral-line targets where there were existing MOSDEF spectra (COSMOS-19439 and COSMOS-19752), we predicted the [O III]$\lambda 4364$ flux based on [O III]$\lambda 5008$ flux as well as T_e predictions. For COSMOS-19439 and COSMOS-19753, we predicted auroral [O III] line fluxes in the ranges of $0.8 - 1.9 \times 10^{-18}$ and $2.1 - 5.0 \times 10^{-18}$ erg s^{-1} cm^{-2} respectively. Since the 2σ upper limits are above our lowest line flux predictions, this suggests that the observations did not reach the required depth in the 10 combined hours of integration. This comparison demonstrates the limitations of 10-m-class ground-based observatories in this area of study and highlights the importance of JWST in building representative galaxy samples moving forward.

4.2. *Insights from [O I] emission*

We present the properties of our sample of galaxies in the [O III]$\lambda 5008$/Hβ vs. [N II]$\lambda 6585$/Hα, [S II]$\lambda\lambda 6716, 6731$/H$\alpha$, and [O I]$\lambda 6302$/H$\alpha$ BPT diagrams shown in Figure 5. In all diagrams, local Sloan Digital Sky Survey (SDSS; York et al. 2000; Abazajian et al. 2009) galaxies are shown as grayscale, two-dimensional histograms. A sample of local H II regions from the literature (see Sanders et al. 2017) is shown
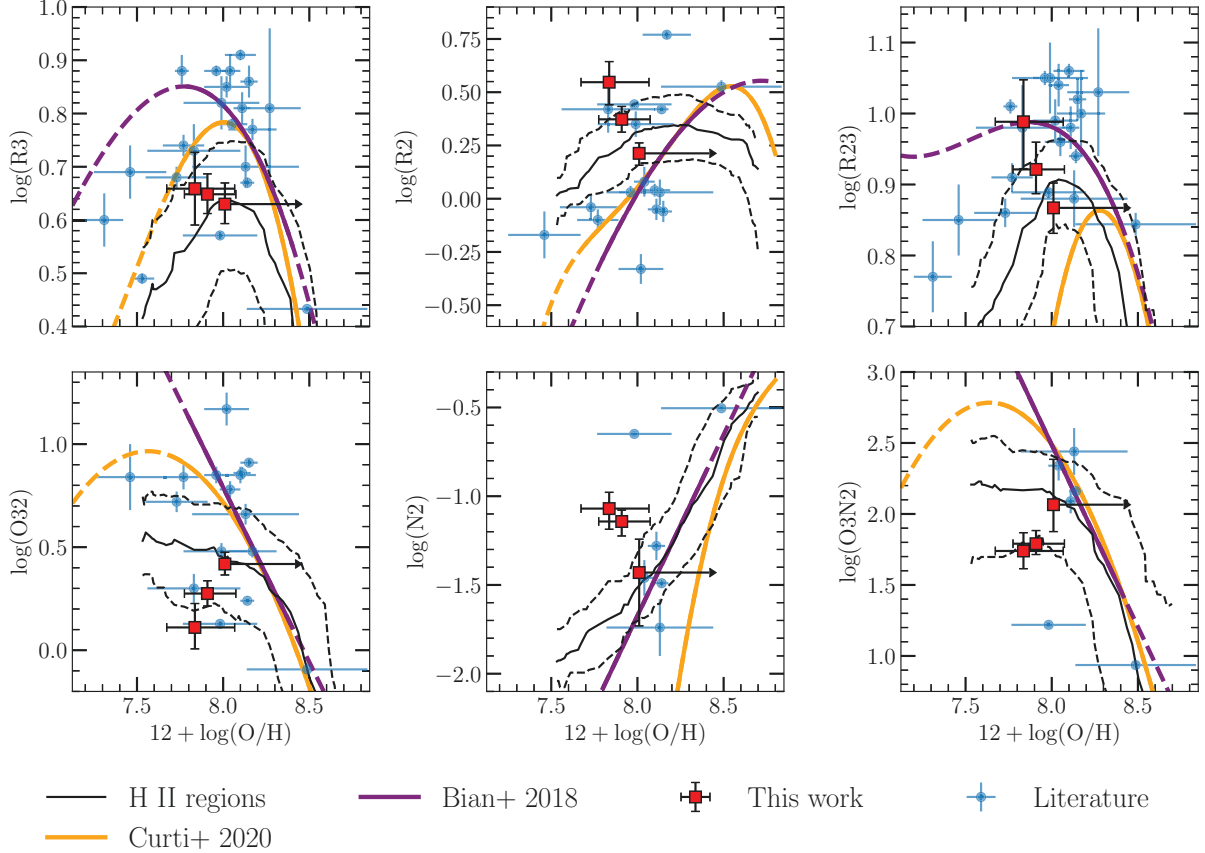
Figure 4. Comparison of the direct oxygen abundance measurements of our stacks with strong-line indicators from Curti et al. (2020) in orange and Bian et al. (2018) in purple. Strong-line indicators are plotted in solid lines over their quoted metallicity ranges, and extrapolations are shown by dashed lines. We also display $z > 1$ galaxies from the literature with direct oxygen abundance measurements as blue points (see Sanders et al. 2020, 2023b). Finally, we show the median relation of local H II regions (see Sanders et al. 2017) as a solid black curve, with the 1σ spread illustrated as black dotted curves.

as a set of magenta points with an accompanying running median and a 1σ shaded region. In the [N II] BPT diagram, we plot the [O III] auroral targets as well as the [O I] composite spectra. We see that the [O III] auroral sample (represented by squares) consists of high-excitation galaxies ($\log([O\,III]\lambda5008/H\beta) \gtrsim 0.5$) and skews toward higher [O III]/Hβ at fixed [N II]/Hα compared to the $z \sim 1.5$ and $z \sim 2.3$ samples from Shapley et al. (2019). When compared to H II regions in the literature, the auroral targets are $\sim$0.1 dex higher in $\log([N\,II]\lambda6585/H\alpha)$ than the median locus of H II regions at fixed $\log([O\,III]/H\beta)$. The characteristics are similar for the $z \sim 2.5$ [O III] auroral galaxy in the [S II]/Hα diagram, where it is offset from the H II regions and Shapley et al. (2019) samples at higher [S II]/Hα and [O III]/Hβ.

We additionally present a novel analysis of galaxies on the [O I] BPT diagram at $z > 1$. Including the filler targets, a total of eight galaxies yielded significant ($>2\sigma$) [O I]$\lambda6302$ detections, with two of the auroral [O III] tar-

gets (COSMOS-19753 and GOODS-N-6699) yielding detections. In order to understand the general characteristics of the galaxies in regard to the [O I] BPT diagram, we constructed two composite spectra separated by redshift, choosing to include galaxies with coverage of the [O I] lines with the exception of galaxies whose [O I] feature fall on sky lines. These criteria result in two stacks with 13 galaxies in the $1 \le z < 2$ stack and 8 galaxies in the $2 \le z \le 3$ stack. The line ratios associated with these stacks are plotted as "plus" (+) symbols in Figure 5.

We see that these stacks follow a similar trend of relatively high [O III]/Hβ relative to the SDSS sample and high [O I]/Hα relative to the locus of H II regions. There are several factors that can influence the [O I]/Hα ratio in a galaxy, including contributions of DIG, the presence of shocks, and hardness of the ionizing spectrum, the latter of which appears to be relevant in $z > 1$ galaxies (Zhang et al. 2017; Shapley et al. 2019).
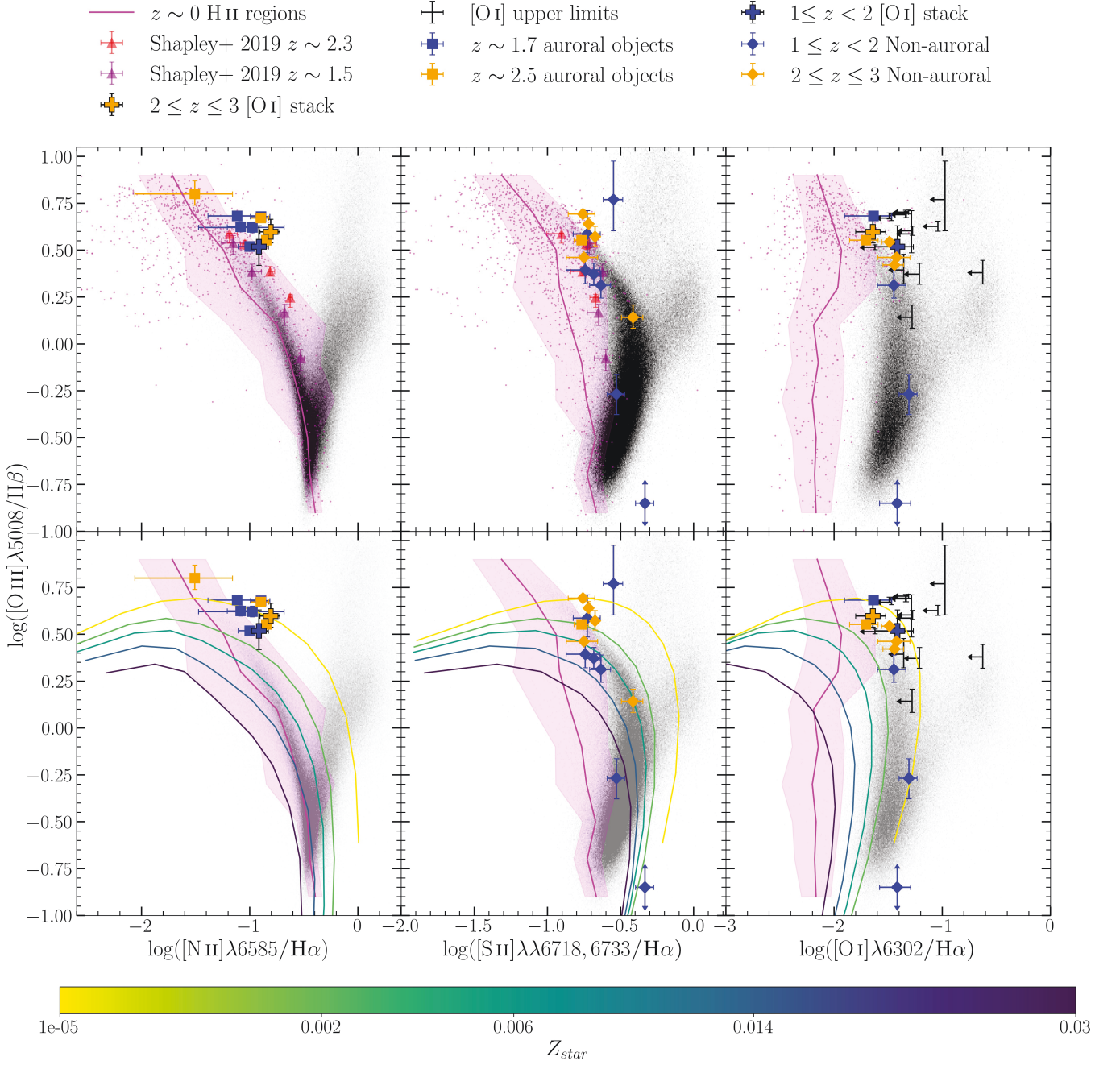
Figure 5. [N II], [S II], and [O I] BPT diagrams showing where the auroral and [O I] galaxy samples from this work lie in relation to SDSS galaxies in the local universe (grayscale, 2D histogram). We also compare the galaxies and stacks from this work to local H II regions from the literature (compiled by Sanders et al. (2017)) and display a running median. The [O III] auroral targets are shown by squares, while the non-[O III]-auroral targets are shown by diamonds. The $1 \leq z < 2$ and $2 \leq z \leq 3$ targets are displayed in blue and orange respectively. For comparison, stacks of $z \sim 1.5$ and $z \sim 2.3$ galaxies from Shapley et al. (2019) are shown as purple and red triangles respectively. Upper limits on [S II] and [O I] detections are shown in black. In the bottom three panels, the same BPT diagrams are shown with CLOUDY photoionization models overlaid. The curves are color-coded by stellar metallicity indicated in the colorbar.

In the bottom three panels of Figure 5, we compare the line ratios from these [O I] stacks to CLOUDY (Ferland et al. 2017) photoionization models following the prescription laid out in Jeong et al. (2020). The models are based on stellar spectra drawn from BPASS (Eldridge et al. 2017; Stanway & Eldridge 2018) where each model curve represents a $10^{8.5}$ year-old stellar population with a constant star-formation history. Along each curve of fixed stellar metallicity (Z_{star}), we vary the ionization parameter and the nebular metallicity according to the Topping et al. (2020a) relation: $\log(U) = -1.06 \times [12 + \log(O/H)] + 5.78$. In both the [N II] and the [O I] BPT diagrams, we find that both the $2 \leq z \leq 3$ and $1 \leq z < 2$ [O I] stacks agree well with the very sub-solar metallicity ($1.0 \times 10^{-5} \lesssim Z_{star} \lesssim 2 \times 10^{-3}$) stellar population curves. Since not all of the galaxies in the [O I] stacks had wavelength coverage of the [S II]$\lambda 6716, 6731$ doublet, we do not include them on the [S II] BPT diagram. Taken together with typical nebular oxygen abundances inferred from the MOSDEF survey (Sanders et al. 2021; Topping et al. 2021), the comparison of these observations with photoionization models supports the picture of harder ionizing spectra from low-metallicity, Fe-poor massive stars driving the line ratios of galaxies at higher redshifts (e.g., Steidel et al. 2016; Strom et al. 2017; Shapley et al. 2019; Sanders et al. 2020; Topping et al. 2020a,b; Runco et al. 2021; Cullen et al. 2021).

Though the harder ionizing spectrum is fully capable of explaining the enhancement in [O I]/Hα in these galaxies, it is also possible that shocks and varying contributions of DIG affect the BPT line ratios. With upcoming spectroscopic observations from JWST, an analysis of these effects may become more robust due to a larger sample of galaxies with a wider range of properties, for which we will also have detections of [O I].

4.3. *Nitrogen abundances*

We additionally comment on the nitrogen abundance patterns displayed by our [O III] auroral galaxy sample. In the context of the star-forming galaxy population at $z \sim 2$, the nitrogen abundances from the stacks are consistent with empirical predictions based on their average stellar masses. For example, Strom et al. (2022) determined the nitrogen abundances for a sample of 195 $z \sim 2$ star-forming galaxies. Their linear fit to this sample predicts a nitrogen abundance of $12 + \log(N/H) = 6.93$ at a stellar mass of $\log(M/M_\odot) = 9.5$ with an intrinsic scatter of 0.33 dex in abundance. Within their respective limits and uncertainties, all three of the stacks as well as GOODS-N-8240 and COSMOS-18812 have nitrogen abundances consistent with this prediction.

As well as analyzing the nitrogen abundance, we discuss the nitrogen to oxygen (N/O) ratio. The N/O ratios of galaxies and H II regions are often used as a probe of the nucleosynthetic origin of nitrogen where, at low metallicity ($12 + \log(O/H) \lesssim 8$), $\log(N/O)$ is fixed at ~ -1.5. This is referred to as the "primary" nitrogen regime since, at low metallicity, the nitrogen yield is tied to those of the α elements (Pilyugin et al. 2010; Pérez-Montero & Contini 2009; Izotov et al. 2006). At higher oxygen abundances, the nitrogen yield increases in proportion to the CNO abundances, and the N/O ratio increases, comprising the "secondary" nitrogen regime. Since the [O III] auroral targets have significantly sub-solar oxygen abundances on average, they should fall within the primary nitrogen regime.

For stacks 1 and 3, where we have constraints on the N/O ratio, we find that their abundance pattern is consistent with those found in local H II regions (e.g., Pilyugin et al. 2010). However, for GOODS-N-8240, we find that its N/O ratio of $\log(N/O) = -0.99^{+0.22}_{-0.23}$ is slightly enhanced given its oxygen abundance of $12 + \log(O/H) = 8.02^{+0.24}_{-0.17}$. Several hypotheses have been put forward to explain the abundance pattern of objects with enhanced N/O, one of which appeals to strong winds from Wolf-Rayet stars enriching the ISM (e.g., Pagel et al. 1986; Brinchmann et al. 2008; Masters et al. 2014). A more detailed analysis is required to determine the exact source of nitrogen enhancement in this target.

Another point of interest in studying the N/O ratio is to investigate its effects on trends in the [N II] BPT diagram across cosmic time. Specifically, if there are significant differences between the N/O vs. O/H ratio at high redshifts compared to low-redshift observations, then an evolving N/O abundance pattern may play an important role in interpreting diagnostic line ratios involving nitrogen and oxygen (Curti et al. 2022; Hayden-Pawson et al. 2022). Because the stacks are consistent with the local N/O vs. O/H relation, there does not appear to be strong evidence for an evolution in the N/O ratio in this sample, though GOODS-N-8240 does represent an outlier in this regard.

5. CONCLUSIONS

We present an ultra deep rest-optical spectroscopic analysis of several $z > 1$, high-excitation galaxies with up to 10 hours of integration time in some bands, and we analyze their excitation properties as well as their oxygen abundances. We selected eight galaxies with strong nebular [O III] emission and high predicted electron temperatures to maximize the chance of detecting the [O III]$\lambda 4364$ emission line. We detected [O III]$\lambda 4364$ in two targets, and we chose to stack the eight [O III]-

auroral-selected galaxies to observe their general characteristics. Additionally, eight of the galaxies that were not targeted for auroral oxygen emission lines yielded [O I] detections, enabling the first analysis of high-redshift galaxies in this parameter space. Here are the key conclusions from this work:

1. When comparing the oxygen abundnces of the auroral-target stacks and galaxies in the literature on the strong-line indicator diagrams, we find that the stacks from this analysis are qualitatively consistent with the distribution found in the literature in both oxygen abundance and strong-line ratio. In general, it is difficult to say with a small sample size whether the Curti et al. (2020) or Bian et al. (2018) curves better describe galaxies at $z > 1$. In the case of $\log(R_{23})$ and $\log(N_2)$, this may be the case. While the current sample size is limited, these results indicate that stacking analyses are promising.

2. When stacking together the galaxies with [O I] coverage (both auroral and non-auroral targets), we find that galaxies typically lie at higher [O I]/Hα at fixed [O III]/Hβ relative to the median locus of local H II regions. This offset is consistent with photoionization models with low-metallicity $(1.0 \times 10^{-5} \lesssim Z_{star} \lesssim 2 \times 10^{-3})$ stellar populations, supporting the picture that the line ratios in $z > 1$ galaxies are driven by harder ionizing spectra at fixed nebular oxygen abundance.

3. The N/O abundances of the [O III] auroral stacks suggests that the nitrogen enrichment in our galaxy sample at $z \sim 2$ is of primary origin and is consistent with the N/O vs. O/H primary abundance pattern seen in local H II regions. Though the N/O abundance of GOODS-N-8240 is enhanced given its oxygen abundance, we do not find evidence that the line ratios in our galaxy sample are driven by an evolving N/O ratio with cosmic time.

The results of this analysis demonstrate the limits of 10-m-class ground-based facilities in the realm of nebular metallicity studies of galaxies at cosmic noon. Given that 10 hours of total integration time was still not enough to reach the required depth to consistently detect the [O III]$\lambda4364$ line in all of the targets, we emphasize the importance of more sensitive facilities such as JWST and future 30-m-class observatories to make advances in this area of study. To date, JWST has already yielded a high number of auroral-line detections out to $z \sim 8$ (e.g., Curti et al. 2023; Williams et al. 2022; Nakajima et al. 2023; Tang et al. 2023; Sanders et al. 2023a). It is already playing an instrumental role in building up the sample of auroral-line measurements at cosmic noon and enabling improvements in strong-line metallicity calibrations at high redshfits.

Facilities: Keck (MOSFIRE)

Software: Astropy (Astropy Collaboration et al. 2018), IDL (Landsman 1993)

REFERENCES

Abazajian, K. N., Adelman-McCarthy, J. K., Agüeros, M. A., et al. 2009, ApJS, 182, 543, doi: 10.1088/0067-0049/182/2/543

Andrews, B. H., & Martini, P. 2013, ApJ, 765, 140, doi: 10.1088/0004-637X/765/2/140

Asplund, M., Grevesse, N., Sauval, A. J., & Scott, P. 2009, ARA&A, 47, 481, doi: 10.1146/annurev.astro.46.060407.145222

Astropy Collaboration, Price-Whelan, A. M., Sipőcz, B. M., et al. 2018, AJ, 156, 123, doi: 10.3847/1538-3881/aabc4f

Baldwin, J. A., Phillips, M. M., & Terlevich, R. 1981, PASP, 93, 5, doi: 10.1086/130766

Berg, D. A., Pogge, R. W., Skillman, E. D., et al. 2020, ApJ, 893, 96, doi: 10.3847/1538-4357/ab7eab

Bian, F., Kewley, L. J., & Dopita, M. A. 2018, ApJ, 859, 175, doi: 10.3847/1538-4357/aabd74

Brinchmann, J., Kunth, D., & Durret, F. 2008, A&A, 485, 657, doi: 10.1051/0004-6361:200809783

Campbell, A., Terlevich, R., & Melnick, J. 1986, MNRAS, 223, 811, doi: 10.1093/mnras/223.4.811

16

Cardelli, J. A., Clayton, G. C., & Mathis, J. S. 1989, ApJ, 345, 245, doi: 10.1086/167900

Chabrier, G. 2003, PASP, 115, 763, doi: 10.1086/376392

Conroy, C., & Gunn, J. E. 2010, FSPS: Flexible Stellar Population Synthesis, Astrophysics Source Code Library, record ascl:1010.043. http://ascl.net/1010.043

Croxall, K. V., Pogge, R. W., Berg, D. A., Skillman, E. D., & Moustakas, J. 2015, ApJ, 808, 42, doi: 10.1088/0004-637X/808/1/42

Cullen, F., Shapley, A. E., McLure, R. J., et al. 2021, MNRAS, 505, 903, doi: 10.1093/mnras/stab1340

Curti, M., Cresci, G., Mannucci, F., et al. 2017, MNRAS, 465, 1384, doi: 10.1093/mnras/stw2766

Curti, M., Mannucci, F., Cresci, G., & Maiolino, R. 2020, MNRAS, 491, 944, doi: 10.1093/mnras/stz2910

Curti, M., Hayden-Pawson, C., Maiolino, R., et al. 2022, MNRAS, 512, 4136, doi: 10.1093/mnras/stac544

Curti, M., D'Eugenio, F., Carniani, S., et al. 2023, MNRAS, 518, 425, doi: 10.1093/mnras/stac2737

Davé, R., Finlator, K., & Oppenheimer, B. D. 2012, MNRAS, 421, 98, doi: 10.1111/j.1365-2966.2011.20148.x

Davé, R., Rafieferantsoa, M. H., Thompson, R. J., & Hopkins, P. F. 2017, MNRAS, 467, 115, doi: 10.1093/mnras/stx108

De Rossi, M. E., Bower, R. G., Font, A. S., Schaye, J., & Theuns, T. 2017, MNRAS, 472, 3354, doi: 10.1093/mnras/stx2158

Dopita, M. A., Sutherland, R. S., Nicholls, D. C., Kewley, L. J., & Vogt, F. P. A. 2013, ApJS, 208, 10, doi: 10.1088/0067-0049/208/1/10

Eldridge, J. J., Stanway, E. R., Xiao, L., et al. 2017, PASA, 34, e058, doi: 10.1017/pasa.2017.51

Erb, D. K., Shapley, A. E., Pettini, M., et al. 2006, ApJ, 644, 813, doi: 10.1086/503623

Ferland, G. J., Chatzikos, M., Guzmán, F., et al. 2017, RMxAA, 53, 385, doi: 10.48550/arXiv.1705.10877

Freeman, W. R., Siana, B., Kriek, M., et al. 2019, ApJ, 873, 102, doi: 10.3847/1538-4357/ab0655

Garnett, D. R. 1992, AJ, 103, 1330, doi: 10.1086/116146

Grogin, N. A., Kocevski, D. D., Faber, S. M., et al. 2011, ApJS, 197, 35, doi: 10.1088/0067-0049/197/2/35

Guo, Y., Koo, D. C., Lu, Y., et al. 2016, ApJ, 822, 103, doi: 10.3847/0004-637X/822/2/103

Hayden-Pawson, C., Curti, M., Maiolino, R., et al. 2022, MNRAS, 512, 2867, doi: 10.1093/mnras/stac584

Heintz, K. E., Giménez-Arteaga, C., Fujimoto, S., et al. 2022, arXiv e-prints, arXiv:2212.06877. https://arxiv.org/abs/2212.06877

Izotov, Y. I., Stasińska, G., Meynet, G., Guseva, N. G., & Thuan, T. X. 2006, A&A, 448, 955, doi: 10.1051/0004-6361:20053763

Jeong, M.-S., Shapley, A. E., Sanders, R. L., et al. 2020, ApJL, 902, L16, doi: 10.3847/2041-8213/abba7a

Kewley, L. J., & Ellison, S. L. 2008, ApJ, 681, 1183, doi: 10.1086/587500

Koekemoer, A. M., Faber, S. M., Ferguson, H. C., et al. 2011, ApJS, 197, 36, doi: 10.1088/0067-0049/197/2/36

Kriek, M., van Dokkum, P. G., Labbé, I., et al. 2009, ApJ, 700, 221, doi: 10.1088/0004-637X/700/1/221

Kriek, M., Shapley, A. E., Reddy, N. A., et al. 2015, ApJS, 218, 15, doi: 10.1088/0067-0049/218/2/15

Landsman, W. B. 1993, in Astronomical Society of the Pacific Conference Series, Vol. 52, Astronomical Data Analysis Software and Systems II, ed. R. J. Hanisch, R. J. V. Brissenden, & J. Barnes, 246

Lequeux, J., Peimbert, M., Rayo, J. F., Serrano, A., & Torres-Peimbert, S. 1979, A&A, 80, 155

Leung, G. C. K., Coil, A. L., Azadi, M., et al. 2017, ApJ, 849, 48, doi: 10.3847/1538-4357/aa9024

Luridiana, V., Morisset, C., & Shaw, R. A. 2015, A&A, 573, A42, doi: 10.1051/0004-6361/201323152

Ly, C., Malkan, M. A., Rigby, J. R., & Nagao, T. 2016, ApJ, 828, 67, doi: 10.3847/0004-637X/828/2/67

Ma, X., Hopkins, P. F., Faucher-Giguère, C.-A., et al. 2016, MNRAS, 456, 2140, doi: 10.1093/mnras/stv2659

Maiolino, R., Nagao, T., Grazian, A., et al. 2008, A&A, 488, 463, doi: 10.1051/0004-6361:200809678

Mannucci, F., Cresci, G., Maiolino, R., Marconi, A., & Gnerucci, A. 2010, MNRAS, 408, 2115, doi: 10.1111/j.1365-2966.2010.17291.x

Mannucci, F., Cresci, G., Maiolino, R., et al. 2009, MNRAS, 398, 1915, doi: 10.1111/j.1365-2966.2009.15185.x

Masters, D., McCarthy, P., Siana, B., et al. 2014, ApJ, 785, 153, doi: 10.1088/0004-637X/785/2/153

McLean, I. S., Steidel, C. C., Epps, H. W., et al. 2012, in Society of Photo-Optical Instrumentation Engineers (SPIE) Conference Series, Vol. 8446, Ground-based and Airborne Instrumentation for Astronomy IV, ed. I. S. McLean, S. K. Ramsay, & H. Takami, 84460J, doi: 10.1117/12.924794

Momcheva, I. G., Brammer, G. B., van Dokkum, P. G., et al. 2016, ApJS, 225, 27, doi: 10.3847/0067-0049/225/2/27

Muzzin, A., Marchesini, D., van Dokkum, P. G., et al. 2009, ApJ, 701, 1839, doi: 10.1088/0004-637X/701/2/1839

Nakajima, K., Ouchi, M., Isobe, Y., et al. 2023, arXiv e-prints, arXiv:2301.12825, doi: 10.48550/arXiv.2301.12825

Nakajima, K., Ouchi, M., Xu, Y., et al. 2022, ApJS, 262, 3, doi: 10.3847/1538-4365/ac7710

Pagel, B. E. J., Terlevich, R. J., & Melnick, J. 1986, PASP, 98, 1005, doi: 10.1086/131862

Peimbert, M. 1967, ApJ, 150, 825, doi: 10.1086/149385

Peimbert, M., Peimbert, A., & Delgado-Inglada, G. 2017, PASP, 129, 082001, doi: 10.1088/1538-3873/aa72c3

Peng, Y.-j., & Maiolino, R. 2014, MNRAS, 443, 3643, doi: 10.1093/mnras/stu1288

Pérez-Montero, E. 2017, PASP, 129, 043001, doi: 10.1088/1538-3873/aa5abb

Pérez-Montero, E., & Contini, T. 2009, MNRAS, 398, 949, doi: 10.1111/j.1365-2966.2009.15145.x

Pilyugin, L. S., & Grebel, E. K. 2016, MNRAS, 457, 3678, doi: 10.1093/mnras/stw238

Pilyugin, L. S., Vílchez, J. M., & Thuan, T. X. 2010, ApJ, 720, 1738, doi: 10.1088/0004-637X/720/2/1738

Reddy, N. A., Kriek, M., Shapley, A. E., et al. 2015, ApJ, 806, 259, doi: 10.1088/0004-637X/806/2/259

Reddy, N. A., Shapley, A. E., Sanders, R. L., et al. 2018, ApJ, 869, 92, doi: 10.3847/1538-4357/aaed1e10.48550/arXiv.1811.11767

Rogers, N. S. J., Skillman, E. D., Pogge, R. W., et al. 2021, ApJ, 915, 21, doi: 10.3847/1538-4357/abf8b9

Runco, J. N., Shapley, A. E., Sanders, R. L., et al. 2021, MNRAS, 502, 2600, doi: 10.1093/mnras/stab119

Sanders, R. L., Shapley, A. E., Topping, M. W., Reddy, N. A., & Brammer, G. B. 2023a, arXiv e-prints, arXiv:2303.08149, doi: 10.48550/arXiv.2303.08149

Sanders, R. L., Shapley, A. E., Zhang, K., & Yan, R. 2017, ApJ, 850, 136, doi: 10.3847/1538-4357/aa93e4

Sanders, R. L., Shapley, A. E., Reddy, N. A., et al. 2020, MNRAS, 491, 1427, doi: 10.1093/mnras/stz3032

Sanders, R. L., Shapley, A. E., Jones, T., et al. 2021, ApJ, 914, 19, doi: 10.3847/1538-4357/abf4c1

Sanders, R. L., Shapley, A. E., Clarke, L., et al. 2023b, ApJ, 943, 75, doi: 10.3847/1538-4357/aca9cc

Shapley, A. E., Reddy, N. A., Kriek, M., et al. 2015, ApJ, 801, 88, doi: 10.1088/0004-637X/801/2/88

Shapley, A. E., Sanders, R. L., Shao, P., et al. 2019, ApJL, 881, L35, doi: 10.3847/2041-8213/ab385a

Shivaei, I., Reddy, N. A., Shapley, A. E., et al. 2015, ApJ, 815, 98, doi: 10.1088/0004-637X/815/2/98

Skelton, R. E., Whitaker, K. E., Momcheva, I. G., et al. 2014, ApJS, 214, 24, doi: 10.1088/0067-0049/214/2/24

Speagle, J. S., Steinhardt, C. L., Capak, P. L., & Silverman, J. D. 2014, ApJS, 214, 15, doi: 10.1088/0067-0049/214/2/15

Stanway, E. R., & Eldridge, J. J. 2018, MNRAS, 479, 75, doi: 10.1093/mnras/sty1353

Steidel, C. C., Strom, A. L., Pettini, M., et al. 2016, ApJ, 826, 159, doi: 10.3847/0004-637X/826/2/159

Steidel, C. C., Rudie, G. C., Strom, A. L., et al. 2014, ApJ, 795, 165, doi: 10.1088/0004-637X/795/2/165

Strom, A. L., Rudie, G. C., Steidel, C. C., & Trainor, R. F. 2022, ApJ, 925, 116, doi: 10.3847/1538-4357/ac38a3

Strom, A. L., Steidel, C. C., Rudie, G. C., et al. 2017, ApJ, 836, 164, doi: 10.3847/1538-4357/836/2/164

Tang, M., Stark, D. P., Chevallard, J., & Charlot, S. 2019, MNRAS, 489, 2572, doi: 10.1093/mnras/stz2236

Tang, M., Stark, D. P., Chen, Z., et al. 2023, arXiv e-prints, arXiv:2301.07072, doi: 10.48550/arXiv.2301.07072

Topping, M. W., Shapley, A. E., Reddy, N. A., et al. 2020a, MNRAS, 495, 4430, doi: 10.1093/mnras/staa1410

—. 2020b, MNRAS, 499, 1652, doi: 10.1093/mnras/staa2941

Topping, M. W., Shapley, A. E., Sanders, R. L., et al. 2021, MNRAS, 506, 1237, doi: 10.1093/mnras/stab179310.48550/arXiv.2103.09245

Toribio San Cipriano, L., García-Rojas, J., Esteban, C., Bresolin, F., & Peimbert, M. 2016, MNRAS, 458, 1866, doi: 10.1093/mnras/stw397

Torrey, P., Vogelsberger, M., Marinacci, F., et al. 2019, MNRAS, 484, 5587, doi: 10.1093/mnras/stz243

Tremonti, C. A., Heckman, T. M., Kauffmann, G., et al. 2004, ApJ, 613, 898, doi: 10.1086/423264

Tumlinson, J., Peeples, M. S., & Werk, J. K. 2017, ARA&A, 55, 389, doi: 10.1146/annurev-astro-091916-055240

Veilleux, S., & Osterbrock, D. E. 1987, ApJS, 63, 295, doi: 10.1086/191166

Williams, H., Kelly, P. L., Chen, W., et al. 2022, arXiv e-prints, arXiv:2210.15699, doi: 10.48550/arXiv.2210.15699

Yabe, K., Ohta, K., Akiyama, M., et al. 2015, PASJ, 67, 102, doi: 10.1093/pasj/psv079

York, D. G., Adelman, J., Anderson, John E., J., et al. 2000, AJ, 120, 1579, doi: 10.1086/301513

Zahid, H. J., Dima, G. I., Kudritzki, R.-P., et al. 2014, ApJ, 791, 130, doi: 10.1088/0004-637X/791/2/130

Zahid, H. J., Kewley, L. J., & Bresolin, F. 2011, ApJ, 730, 137, doi: 10.1088/0004-637X/730/2/137

Zhang, K., Yan, R., Bundy, K., et al. 2017, MNRAS, 466, 3217, doi: 10.1093/mnras/stw3308